

Measurements and predictions of light scattering by clear coatings

Mary E. McKnight, Theodore V. Vorburger, Egon Marx, Maria E. Nadal, P. Yvonne Barnes, and Michael A. Galler

Comparisons are made between calculated and measured angle-resolved light-scattering distributions from clear dielectric isotropic epoxy coatings over a range of rms roughness conditions, resulting in strongly specular scattering to diffuse scattering characteristics. Calculated distributions are derived from topography measurements performed with interferometric microscopes. Two methods of calculation are used. One determines the intensity of scattered light waves with a phase integral in the Kirchhoff approximation. The other is based on the reflection of light rays by locally flat surfaces. The angle-resolved scattering distributions for the coatings are measured with the spectral trifunction automated reference reflectometer (STARR) developed by the National Institute of Standards and Technology. Comparisons between measured and calculated results are shown for three surfaces with rms roughness values of approximately 3, 150, and 800 nm for an angle of incidence of 20°.

OCIS codes: 290.5880, 180.3170, 160.4890, 120.5700, 120.6660, 080.2720.

1. Introduction

Appearance is a critical performance parameter for most industries, including automotive, textile, paper, and plastic. For example, the color and appearance of automobiles is reported to be the major influence in approximately half of car purchases.¹ The visibility of warning signs and camouflaged objects also depends on the optical properties of the materials. Furthermore, continuing demands for new materials and manufacturing processes, as well as customer expectations for improved appearance quality, create a need for advanced appearance measurements and models.

This study is part of an appearance project² at the National Institute of Standards and Technology (NIST) whose purpose is to develop advanced methods for appearance characterization and predictive image rendering of surfaces through a systems approach by use of optical metrology, descriptions of surface and subsurface microstructure, mathematical modeling, and computer rendering. The first step of the project is to relate the optical properties of the raw materials to the microstructure of the man-

ufactured material. The next steps are to characterize the microstructure, to measure the optical reflectance properties of the manufactured materials, and to model mathematically the optical reflectance properties based on the microstructure. Finally, scientifically accurate rendering models are used to create images of objects with the measured or the modeled reflectance values. In this way, relationships between material properties and optical reflectance can be developed and used to predict the appearance of materials.

The first samples chosen to demonstrate the approach consisted of clear dielectric epoxy coatings on a black-glass substrate. Surface scattering is dominant in these samples. Pigmented coatings in which both bulk and surface scattering are important are being used in the next phase of the project. The clear coating samples were fabricated to test the model over a range of rms roughness conditions, resulting in strongly specular scattering to diffuse scattering characteristics. The angle-resolved light-scattering measurements were performed with the NIST spectral trifunction automated reference reflectometer (STARR).³ The topographical data used in the optical scattering models were determined with interferometric microscopy. Two methods were used to calculate angle-resolved light scattering for comparison with the corresponding measured values. One method determined the intensity of scattered light waves by use of a phase integral in the Kirchhoff

The authors are with the National Institute of Standards and Technology, Gaithersburg, Maryland 20899. M. McKnight's e-mail address is mary.mcknight@nist.gov.

Received 18 September 2000; revised manuscript received 9 February 2001.

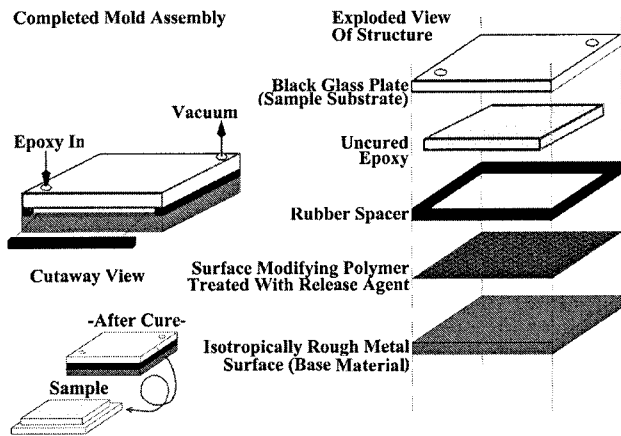


Fig. 1. Schematic diagram illustrating fabrication of clear-epoxy samples with controlled roughness.

approximation.⁴ The other method was based on the reflection of light rays by locally flat surfaces (see, for example, Ref. 5). Bendler *et al.*⁶ carried out a comparable experiment in which they calculated an absolute scattering distribution for light waves for a perfectly conducting surface, using a statistical model of the surface. This study is different in that the dielectric sample surfaces transmit light in addition to scattering light and a topographical map of the surface is used to calculate the scattered light.

The study described in this paper serves as a test of three independent procedures: the surface measurements, the optical scattering measurements, and the optical scattering calculations. Assuming that the two types of measurement are accurate, agreement between the calculated results and the scattering measurements thus serves as a demonstration of the validity of different approximations used in reflectance theory. The agreement also validates calculations done in the ray approximation, which were used in a demonstration of computer rendering based on the reflectance of these surfaces.⁷

The simulation of the measured intensities by the phase integral involves a number of constant factors that are difficult to determine, including one that takes into account the refraction at the dielectric surface. The ray counting method does not provide an absolute intensity either. Thus angular distributions of measured and computed light intensities that have been normalized to 1 in the specular direction were compared.

2. Experiment

A. Sample Preparation

The samples for this study were made of a clear 100% solid amine-cured epoxy coating on a black-glass substrate. Samples were prepared, as illustrated in Fig. 1, by means of casting the coating against 50 mm × 50 mm molds of varying roughness. Black glass (Schott Glass,⁸ NG-1, 3-mm thickness) was used as the mold to prepare the sample with the smoothest surface. The remaining molds were pre-

pared with a matte finished, steel panel (rms roughness of ~1 μm) as the base material. The roughness of the base material was modified by spin coating with a solution containing a surface-modifying polymer. Polymer solutions with volume solid fractions increasing from 10% to 45% were used to prepare molds systematically with decreasing rms roughness values from approximately 800 to 100 nm, as estimated from mechanical (stylus) profiling data.⁹ The roughness of the molds decreased with increasing concentration of the polymeric solution, as predicted.¹⁰

Sets of epoxy-coating samples were prepared by means of treating each mold with a release agent, constructing sides ~1.3 mm thick with a rubber gasket material, and clamping a black-glass substrate material against the mold with spring-loaded clamps (see Fig. 1). The assembly was held upright, and the premixed, degassed epoxy coating was introduced through a hole in a bottom corner of the glass. A hole in the opposite corner of the glass substrate served as a vent. By means of forcing epoxy into the lower hole, trapped air bubbles in the coating were minimized. Next, the epoxy was heat cured according to the manufacturer's instructions, and then the whole was disassembled. The actual size of the cured-coating sample was approximately 35 mm × 35 mm, smaller than the black-glass substrate, because of the gasket and the holes drilled in the substrate.

Except for the sample cast against black glass, estimates of the roughness of the representative samples were obtained from stylus profile measurements. Samples taken from the set corresponding to stylus roughnesses of 640 nm (sample A) and 115 nm (sample B) and the black-glass replicate (sample C) were selected for the study.

The index of refraction of the black substrate glass and the epoxy coating are 1.52 and 1.55 at a wavelength of 587.6 nm, respectively. The estimated expanded uncertainty of the index of refraction values is less than 0.01. Because the difference in the refractive indices of the epoxy and the glass is slight, the intensity of the light reflected from the glass-coating interface is small compared with that of the light scattered from the surface (~0.01% for an angle of 20° and ~0.1% for an angle of 60°, estimated with the Fresnel equations).

B. Optical Scattering Measurements

Angle-resolved scattering from rough surfaces is often described with the bidirectional reflectance distribution function (BRDF), which is the ratio of the differential radiance to the differential irradiance.¹¹ Irradiance is the light flux or power incident per unit area, whereas radiance is the light flux scattered from the sample, in a given direction, per unit projected area of the sample viewed from that direction, per unit solid angle. For the case of a nearly collimated incident beam,

$$\text{BRDF} \approx [P_s / (\Omega_s \cos \theta_s)] / P_i \quad (1)$$

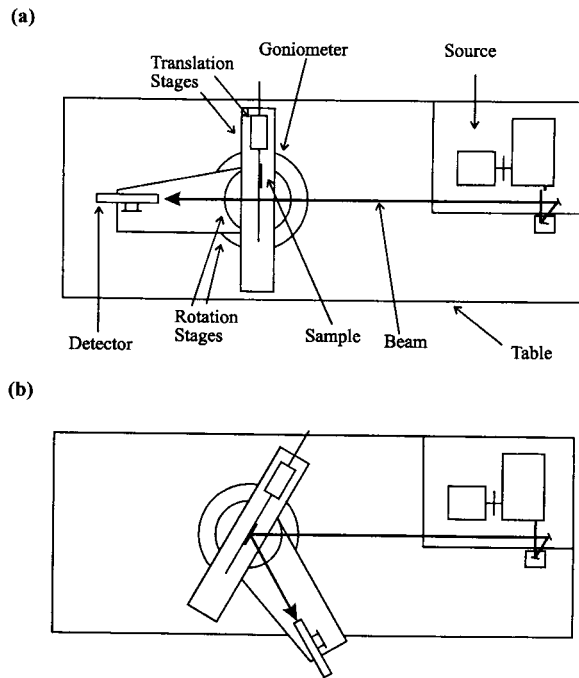


Fig. 2. Schematic diagram of STARR with all the major components labeled in part (a). (a) Incident-flux measurement, (b) reflected-flux measurement.

where the indices i and s stand for incident and scattered quantities, respectively; P is flux or power; Ω is the solid angle; and θ is the polar angle. Reflectance ρ is defined as the ratio of the powers

$$\rho = P_s/P_i = \text{BRDF} \cdot \Omega_s \cos \theta_s. \quad (2)$$

Absolute measurements of in-plane bidirectional scattering were performed with STARR^{3,12} at NIST. Figure 2 is a schematic of the instrument. The incident radiant flux is a collimated, monochromatic, polarized beam with a diameter of 14 mm and bandwidth of 10 nm. For bidirectional measurements, a lens focuses either the collimated incident beam or the image of the front of the sample onto the detector, a silicon photodiode. The sample is positioned either in or out of the incident beam path by use of two orthogonal translation stages. Two rotation stages determine the angle of incidence of the beam on the sample and the viewing angle of the photodiode. The detector assembly rotates around the sample holder at a constant distance of 672.6 mm, measured from the sample rotation axis to the 31.8-mm-diameter aperture stop in the detector. Therefore the detector aperture subtends an angle of approximately 2.7°.

The reflectance is calculated from measurements of the incident and the reflected radiant fluxes. The incident flux is measured with the sample positioned out of the beam path and the receiver positioned to accept the incident beam. The reflected radiant flux is measured with the sample positioned in the beam path with the sample and the detector positioned to measure the reflected flux at the desired geometry.

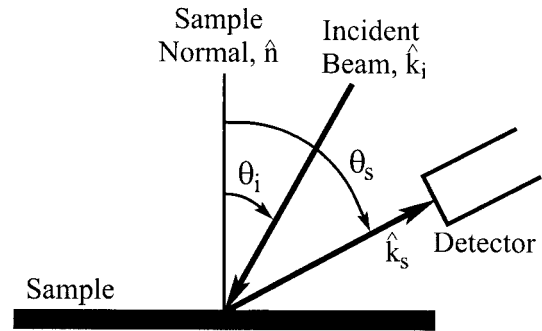


Fig. 3. Convention for incidence and scattering angles.

The angular convention is shown in Fig. 3. The angle of incidence θ_i and the scattering angle θ_s are measured from the normal to the sample. In this convention, the specular direction for an angle of incidence θ_i is along $-\theta_i$.

The reflectance of the each of the three clear-epoxy coating samples and a highly polished black-glass sample were measured at wavelengths of 500, 550, and 600 nm for angle of incidences of 20°, 45°, 60°, and 70° and viewing angles from -75° to 75° in steps of 1°. Results are shown only for 550 nm and, with exception of some measured data of the absolute reflectance, for 20°, because not much additional information is gained from the comparison of calculated and measured relative reflectances for these samples at other wavelengths and angles.

C. Surface Topography Measurements

The surface topographies of the three clear-epoxy coating samples were measured by interferometric microscopy to provide input for the optical scattering calculations. The topography data z are described by a function $\zeta(x, y)$, where ζ represents the height of the surface at a lateral position (x, y) . This is a digital representation in which the x, y positions are linked to pixel elements in the camera of the microscope, which are equally spaced in x and in y . Therefore the point (x, y) can be represented by $(i\Delta x, j\Delta y)$ where i and j are the pixel indices and Δx and Δy are the sampling intervals.

The surfaces of the samples were measured by the technique of scanning white-light interferometric (SWLI) microscopy.^{13,14} A typical SWLI microscope is shown in Fig. 4, taken from Ref. 15. A wideband source of light is collimated and then focused through a beam splitter in a cone of angles around normal incidence. Part of the light proceeds to the sample surface, and part is reflected to the reference surface. The beams reflected by the sample and the reference are recombined and produce optimally strong interference fringes on the camera when the optical path difference between them is zero. The topographic data are recorded as follows. The reference mirror is scanned vertically, and the equal path condition is found for each pixel in the camera. The z positions for the equal path condition are a function of the

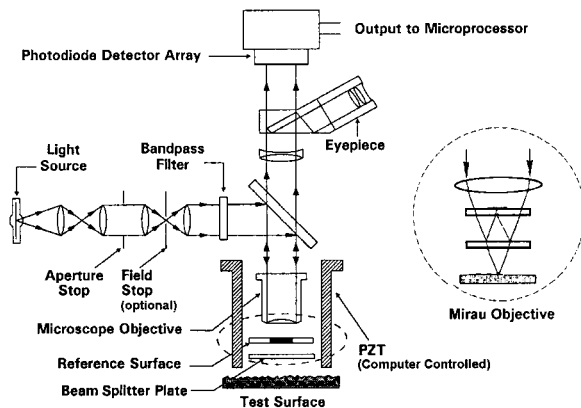


Fig. 4. Schematic diagram of a typical interferometric microscope, which may be used either in the phase-shifting mode or the scanning white-light mode. PZT, piezoelectric transducer

sample surface topography. The z -position data for each pixel (x, y) yields the topographic map $\zeta(x, y)$.

Two different interferometric microscopes,^{8,16,17} located at their respective manufacturer's sites, were used to measure the topographies of samples A and B. The instrument parameters were slightly different for the two microscopes. Table 1 shows the nominal measurement parameters for the two microscopes. For both sets of topography measurements, the area of the sample measured by the STARR was visually positioned under the microscope, and an unblemished area was chosen for the measurement. No attempt was made to relocate the same measured area from one microscope to the other. Sample C was measured subsequently to samples A and B and was significantly smoother. Its surface topography was measured in three areas with a third microscope of the same type as microscope 1 but in the phase-shifting-interferometry (PSI) mode¹⁸ rather than in the SWLI mode. The PSI mode was used because the rms roughness of sample C is approximately at the limit of vertical resolution of SWLI for this microscope, whereas PSI has subnanometer vertical resolution. The PSI technique is similar to SWLI microscopy and has essentially the same schematic diagram. As with SWLI microscopy, the surface topography is measured by continuous measurement of the changes in the

interferometric fringes over the surface as the reference surface is slowly scanned. However, monochromatic light is used, and the surface topography is calculated with a different algorithm than that for SWLI.¹⁹ Table 1 shows the measurement parameters.

3. Light-Scattering Calculations

The intensity of light scattered by a rough surface specified by surface maps was calculated with two different methods. One method is based on the phase integral for the scattered field amplitude in the Kirchhoff approximation as derived by Beckmann.⁴ The second method is based on the specular reflection of light rays by locally flat surfaces. Results were compared with intensities measured by use of STARR.

For the scattering calculations, the surface is represented by a topographic map as described in Subsection 2.C. Light of wavelength λ is assumed to be incident along a direction given by the polar angle θ_i and the azimuthal angle ϕ_i . The derivation of the scattered light intensity assumes that the surface is perfectly conducting, although Beckmann extends the approach to finitely conducting media, such as dielectrics.⁴

In the phase integral approximation, the amplitude of the light scattered by a perfectly conducting rough surface in the direction given by the spherical coordinate angles θ_s and ϕ_s from an incident, monochromatic, electromagnetic plane wave is given by

$$\psi(\theta_i, \phi_i; \theta_s, \phi_s) = [F_3(\theta_i, \phi_i; \theta_s, \phi_s)/A] \int_{\Sigma} \exp[i\mathbf{v}(\theta_i, \phi_i; \theta_s, \phi_s) \cdot \mathbf{r}(x, y)] dx dy, \quad (3)$$

where Σ is the projection of the illuminated region on the xy plane and A its area,

$$F_3(\theta_i, \phi_i; \theta_s, \phi_s) = \frac{1 + \cos \theta_i \cos \theta_s + \sin \theta_i \sin \theta_s \cos(\phi_i - \phi_s)}{\cos \theta_i (\cos \theta_i + \cos \theta_s)}, \quad (4)$$

Table 1. Measurement Parameters for Scanning White-Light Interferometric Microscopes

Parameter	SWLI Microscope 1 ^a	SWLI Microscope 2 ^b	PSI Microscope 3 (same type as 1)
Interferometer configuration	Mirau	Mirau	Mirau
Nominal pixel spacing $\Delta x, \Delta y$	0.796 μm , 0.927 μm	2.25 μm , 2.25 μm	0.409 μm , 0.477 μm
Number of pixels N_x, N_y	736, 480	320, 240	736, 480
Size of Measured area $N_x \Delta x \times N_y \Delta y$	586 $\mu\text{m} \times 445 \mu\text{m}$	720 $\mu\text{m} \times 540 \mu\text{m}$	301 $\mu\text{m} \times 229 \mu\text{m}$
Numerical aperture	0.3	0.3	0.3
Number of measured areas	1	1	3
Samples measured	A and B	A and B	C

^aSee Ref. 16.

^bSee Ref. 17.

$$\begin{aligned} \mathbf{v} = & -k[(\sin \theta_i \cos \phi_i + \sin \theta_s \cos \phi_s)\hat{e}_x \\ & + (\sin \theta_i \sin \phi_i + \sin \theta_s \sin \phi_s)\hat{e}_y \\ & + (\cos \theta_i + \cos \theta_s)\hat{e}_z], \end{aligned} \quad (5)$$

$k = 2\pi/\lambda$. The amplitude has been normalized to that reflected by a flat surface.⁴ It follows that

$$\begin{aligned} \mathbf{v} \cdot \mathbf{r} = & -k[(\sin \theta_i \cos \phi_i + \sin \theta_s \cos \phi_s)x \\ & + (\sin \theta_i \sin \phi_i + \sin \theta_s \sin \phi_s)y \\ & + (\cos \theta_i + \cos \theta_s)\zeta(x, y)]. \end{aligned} \quad (6)$$

Note that the measured three-dimensional topography is used for the calculation with no assumption of surface isotropy and that these equations reduce to those in Ref. 4 if we set $\phi_i = \pi$. The integral in Eq. (3) is approximated by a sum, and a good approximation requires the use of at least ten points per wavelength. However, it is not possible to obtain data at such close intervals with an optical instrument. Therefore a two-dimensional cubic spline was used to interpolate the topographical data on the surface. The interpolated points are chosen not to be equispaced so as to avoid possible problems with scattering by a (numerical) grating. Although STARR has the capability for measurements slightly outside the plane of incidence, for these experiments the detector was scanned only through the plane of incidence. Therefore $\phi_s = \phi_i$ is used in all calculations to simulate this approach. The range of θ_s is extended to negative values by mapping of $(\theta_s, \phi_s) \rightarrow (-\theta_s, \phi_s - \pi)$ for $\phi_s \geq \pi$.

If the illuminated surface is assumed to be a perfectly flat rectangle of sides L_1 and L_2 , Eq. (3) reduces to

$$\begin{aligned} \psi(\theta_i, \phi_i; \theta_s, \phi_s) = & F_3(\theta_i, \phi_i; \theta_s, \phi_s) \text{sinc}(v_x L_1/2) \\ & \times \text{sinc}(v_y L_2/2), \end{aligned} \quad (7)$$

where v_x and v_y are given in Eq. (5). The sinc functions decrease rather slowly with increasing argument, which causes the computed scattered intensity to remain relatively large away from the specular direction, contrary to what happens experimentally. Because an actual light beam does not have a uniform intensity that suddenly drops to zero outside the patch, a beam profile was simulated with a windowing function, $W(x, y)$. Then Eq. (3) becomes

$$\begin{aligned} \psi(\theta_i, \phi_i; \theta_s, \phi_s) = & [F_3(\theta_i, \phi_i; \theta_s, \phi_s)/A] \int_{\Sigma} W(x, y) \\ & \times \exp[i\mathbf{v}(\theta_i, \phi_i; \theta_s, \phi_s) \\ & \cdot \mathbf{r}(x, y)] dx dy. \end{aligned} \quad (8)$$

For a rectangular patch it is assumed that $W(x, y) = W_1(x)W_2(y)$. Through investigations of a number of windows in calculations of light scattered by a sinusoidal surface^{20,21} it was concluded that the test function used by Schwartz in the theory of distributions

gives the best computed results. This windowing function is

$$W(x) = \begin{cases} \exp\{\alpha[1 - L_i^2/(L_i^2 - x^2)]\} & |x| \leq L_i \\ 0 & \text{elsewhere} \end{cases}, \quad (9)$$

for $i = 1, 2$. The value $\alpha = 0.1$ was used in calculations. The windowing function does not have to reflect the actual cross section of the incident beam of light, which covers a much larger region of the sample than the surface map does. It is used here to avoid the numerical problems associated with a discontinuity at the edges of the surface map. The light beam is often assumed to have a Gaussian cross section, but calculations indicate that a Gaussian that remains close to 1 over a sizable fraction of the region of integration will have a jump at the edges that reproduces the problems associated with the rectangular window.^{20,21}

An actual detector collects light over a solid angle. To compare with measured values of the scattered light intensity, the computed values can be integrated over the surface of the detector, or they can be convolved with the measured instrument signature. The first approach requires computing the scattered intensity for a large number of angles, especially when the detector is positioned in the specular direction. The second approach is easier to implement and was used in the calculations described here. The simulated intensity, $\bar{I}(\theta)$, is expressed as the integral of the product of the computed intensity, $I(\theta) = |\psi(\theta)|^2$, and the displaced signature of the instrument or response curve, $I_r(\theta)$, which is given by the unnormalized intensities measured by STARR in the absence of the sample. The simulated intensity then is

$$\bar{I}(\theta) = \int_{-(1/2)\pi}^{(1/2)\pi} I(\theta') I_r(\theta' - \theta) d\theta'. \quad (10)$$

This integration is carried out numerically. The function $I(\theta)$ varies rapidly near the specular direction, which means that the interval $\Delta\theta'$ has to be much smaller in that region than elsewhere. The number of points needed for the integration was determined by means of subdividing the original interval and analyzing the change in the result. If the change was larger than a preset fraction, the interval was again subdivided.

Because this model does not take into account the dielectric constant of the epoxy layer, the intensity of the scattered light can be computed only up to an overall factor. Thus the measured and the calculated intensities were compared by means of normalizing the curves to 1 in the specular direction.

The ray method used to determine the angular distribution of the scattered light is based on the assumption that an incident ray is reflected specularly by the surface, assumed to be locally approximated by a tangent plane.^{5,22} One determines the direction of the normal, \hat{n} , to the surface at a particular point either by performing a least-squares fit of

the distances from the neighboring points to a (tangent) plane through the given point or by fitting a cubic spline to the surface. The method used to compute the normal to the surface had a negligible effect on the resulting intensities. The execution time required for computing an intensity distribution with the ray method is much smaller than the time required for computing phase integrals. Consequently, this method can more easily be used to compute the bidirectional reflectance distribution function for the purpose of computer rendering, requiring intensities for many directions of incidence and scattering.⁷ Computations based on the Kirchhoff approximation can be used to validate those that use the ray approximation.

If \hat{k}_i is in the direction of the incident wave, the direction, \hat{k}'' , of the locally reflected wave is

$$\hat{k}'' = \hat{k}_i - 2(\hat{k}_i \cdot \hat{n})\hat{n}. \quad (11)$$

If the axis of the j th detector position is along the direction of \hat{r}_j , the angle Δ between this axis and the local specular beam is given by

$$\begin{aligned} \cos \Delta = \hat{k}'' \cdot \hat{r}_j = & \sin \theta'' \sin \theta_j \cos(\phi'' - \phi_j) \\ & + \cos \theta'' \cos \theta_j, \end{aligned} \quad (12)$$

where θ'' and ϕ'' are the polar coordinates of \hat{k}'' .

If the computed angle Δ is smaller than the half-aperture of the instrument, the reflected ray falls within the detector, and the count for that detector is incremented by one unit. The approximation to the scattered intensity will then be proportional to the number of counts for the detector. Again the intensity distribution is normalized to 1 in the specular direction. The agreement of intensities obtained in this simple ray optics model with measured results and those obtained from the phase integral shows that a more elaborate ray intensity formula related to the surface curvature obtained in the geometric optics approximation is not needed.

A third method that can be used to compute the scattered light is a numerical solution of the exact integral equation that is equivalent to Maxwell's equations.²³ To simplify the problem, one can assume that a monochromatic plane wave is incident on a rough measured patch embedded in a flat surface of a dielectric half-space. The patch has to be tapered off into the plane. However, the memory requirements are such that only a small subset of the measured surface image can be used in the calculation. Thus calculations using this method were not done. Another commonly used method is the first-order vector theory.²⁴ However, this approximation is valid only if the rms roughness is much less than λ , a requirement that is not true for samples A and B.

4. Results

A. Optical Scattering Measurements

Selected results of the optical scattering measurements are shown in Figs. 5 and 6, where a linear scale

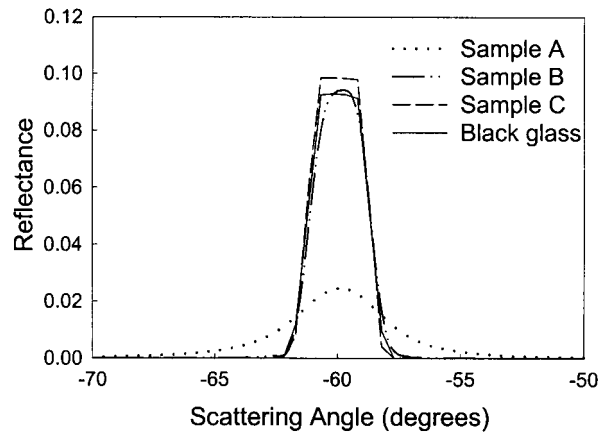


Fig. 5. Measured reflectance as a function of observation (scattering) angle for samples A, B, and C, and for a highly polished black-glass specimen at 550 nm and 60° angle of incidence.

is used for the reflectance. Figure 5 shows the reflectance as a function of scattering angle for a 60° angle of incidence at 550 nm for all the samples and for black glass. The goniodistribution of the reflectance is nearly symmetric about the specular angle, -60°. The light around the specular direction decreases as the surface roughness increases and more diffuse reflection is observed. The refractive index of the clear epoxy is ~2% larger than that of black glass, resulting in an increase of ~7% in specular reflectance, consistent with the measured values shown in Fig. 5.

Figure 6 shows the absolute reflectance for sample B for angles of incidence of 20°, 45°, and 60°. The samples appear more glossy as the angle of incidence increases from 20° to 60°, as predicted by the Fresnel equations, but the shapes of the curves near the specular direction do not depend strongly on the angle.

The isotropy of the samples was investigated by measurement of the absolute specular reflectance as the sample was rotated about the normal of the surface. Since the measured reflectances remain essen-

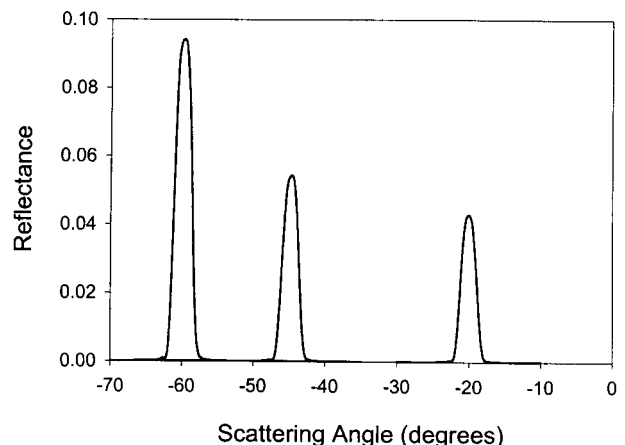


Fig. 6. Measured reflectance of sample B as a function of observation angle for incident angles of 20°, 45°, and 60°.

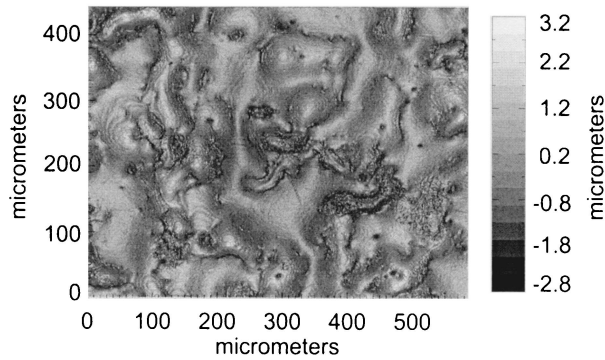


Fig. 7. Surface topography map of sample A as measured by SWLI microscope 1; rms roughness, 805 nm.

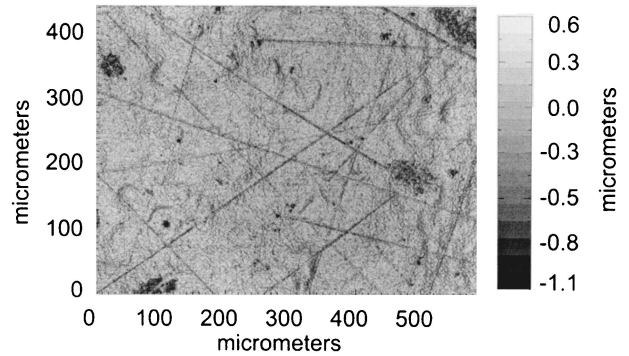


Fig. 9. Surface topography map of sample B as measured by SWLI 1; rms roughness, 201 nm.

tially constant, the epoxy layer is assumed to be isotropic over the 14-mm-diameter illuminated region for the lateral scale relevant to this measurement.

Uncertainties were calculated according to the procedures outlined in Ref. 25. The type A uncertainty components, which are calculated by statistical methods, include source stability and detector noise and result in a relative uncertainty of 0.05%. Type B sources of uncertainty include wavelength, incident and viewing angles, and uniformity of the sample. The relative uncertainty that is due to the type B sources is 0.2%. The expanded uncertainty in the measured reflectance with a coverage factor $k = 2$ is 0.4% at 500 nm.

B. Surface Topography Measurements

Topography maps of the samples are shown in Figs. 7–11. The roughness scale as shown in the vertical bar in each figure was allowed to vary so that features in each image could be displayed clearly. The measured rms roughnesses for the surface of sample A were 805 and 871 nm and for the surface of sample B were 201 and 124 nm for SWLI microscopes 1 and 2, respectively. The difference in rms roughness values suggests that the surfaces vary significantly on the measured lateral scale of ~ 0.5 mm. In addition, scratchlike marks were observed in sample B in the area examined with SWLI microscope 1 but not in the area examined with microscope 2.

The rms roughness values measured with the microscopes are larger than those measured with the stylus-profiling instrument. The difference could be associated with the differences in the bandwidths of the two techniques. The bandwidth of spatial wavelengths in the topography maps extends from the optical resolution of the microscope, ~ 1 μm , to the size of the map itself, approximately 585 or 720 μm , larger than the bandwidth of the stylus measurements (250 μm).

Sample C was measured subsequently. Three areas were measured on this surface, all within the 14-mm-wide area covered by the light-scattering

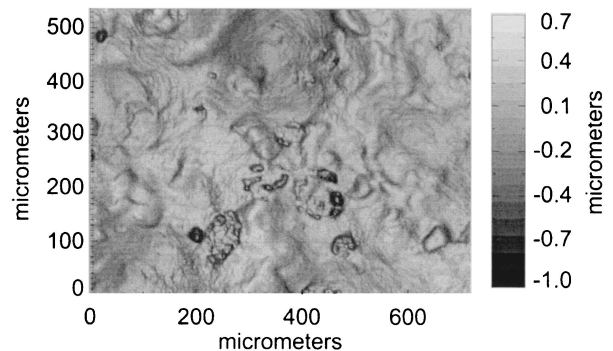


Fig. 10. Surface topography map of sample B as measured by SWLI 2; rms roughness, 124 nm.

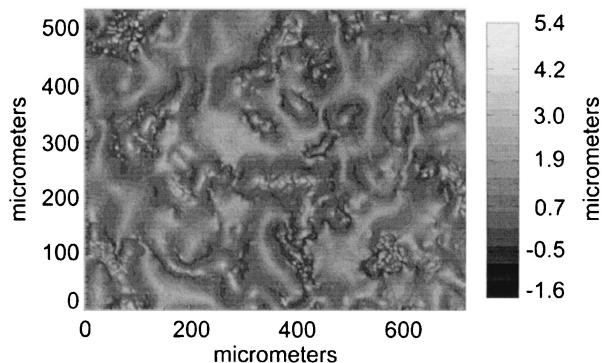


Fig. 8. Surface topography map of sample A as measured by SWLI microscope 2; rms roughness, 871 nm.

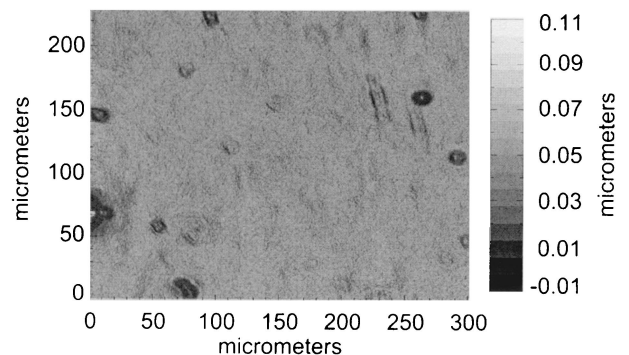


Fig. 11. Typical surface topography map of sample C as measured by PSI microscope of type 1; rms roughness, 5.0 nm.

technique. The measured rms roughnesses of the three measured areas were 5.0, 3.0, and 2.2 nm. The topography map for the area with rms roughness of 5.0 nm is shown in Fig. 11. The variation of these measurements is again due to the nonuniformity of the specimen surface. The standard deviation of the three rms roughness measurements is 1.4 nm, $\sim 41\%$ of the average value of 3.25 nm. The uncertainties arising from the instrument are considerably smaller than this. Notably, in PSI mode, the instrument is calibrated directly against the wavelength of light with a small obliquity correction factor required at the $20\times$ magnification used in this study.

C. Light-Scattering Calculations

Calculations and measurements were performed for a number of angles, but not all results are shown. The results for different angles of incidence are similar in nature.

In Fig. 12 the relative reflectances measured and computed with the phase integral model and the different topography data are compared for incidence angles of 20° for the three samples. The same vertical logarithmic scale for all the graphs was used, and the lower end of the y scale was arbitrarily limited to 1×10^{-6} . The agreement between the measured and the computed intensity distributions is good, especially if one takes into account that the logarithmic scale exaggerates the differences for angles that are farther away from the specular direction. The broadening of the measured scattering distribution with increasing roughness is clearly reproduced by the computed distribution. The computed relative reflectance of sample C differs little from that of a perfectly flat surface.

The effect of the windowing function is shown in Fig. 13. For the roughest sample, sample A, the windowing effect is small, as seen in Fig. 13(a). For the smoother samples, B and C, different types of window give varying intensities at angles away from the specular direction as shown in Figs. 13(b) and 13(c). For sample C the relative reflectance calculated with a rectangular window is significantly above the measured values, which indicates a need to take into account the windowing effect in the calculation. In Fig. 13(b) the computed intensities calculated for azimuthal angles of 90° show some degree of freedom anisotropy at the scale of the surface maps. Because of the preparation method, samples are expected to be isotropic. Measurements of the angular distribution of the scattered light in which the sample was rotated indicate that this is indeed so for a size scale of the order of 14 mm. The measured surface maps could appear less isotropic than the scattering results because fewer local features are measured at the smaller scale of ~ 0.5 mm. Figure 13(b) indicates that the computed scattered intensities differ by an order of magnitude, which also suggests that the better agreement of the intensities computed with a square window with the measured ones is not significant. Samples A and C do not show this anisotropy for the calculated intensities.

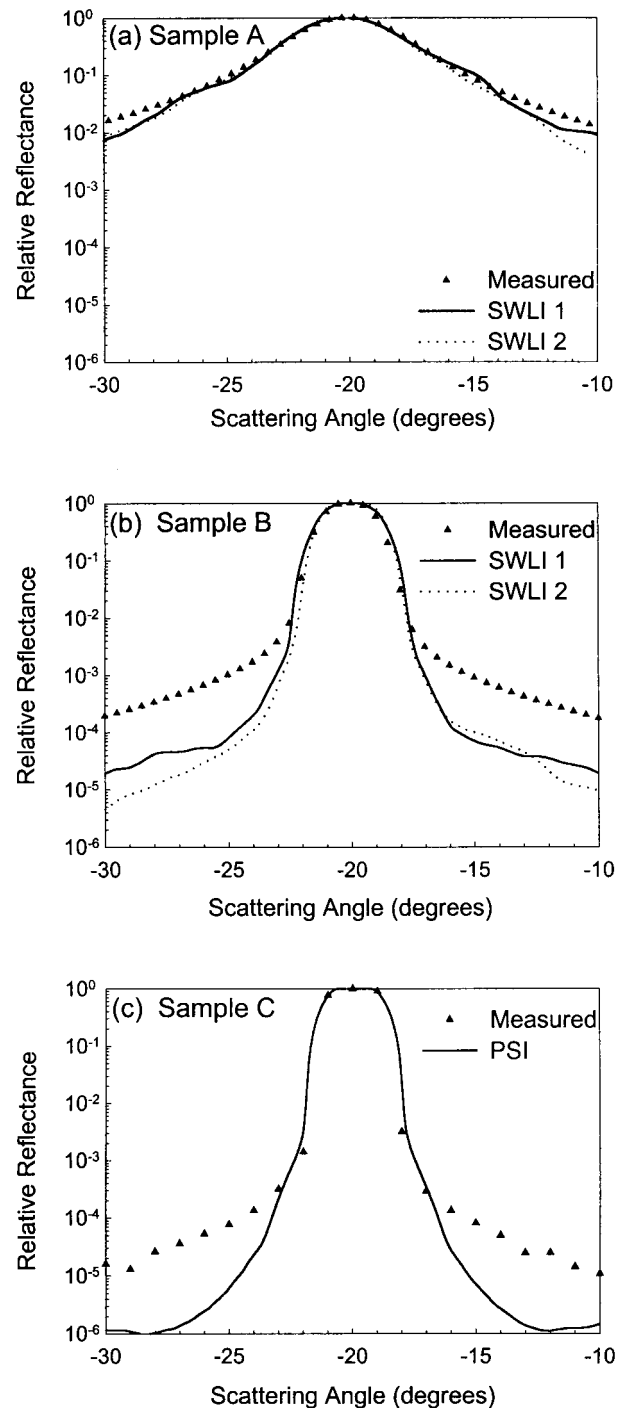


Fig. 12. Comparison between relative reflectance curves as a function of scattering angle, measured and computed with a Schwartz window in the phase integral calculation.

In Fig. 14 the intensity distributions calculated with the phase integral are compared with those obtained by ray scattering with the least-squares-fit algorithm used to calculate the tangent planes. The measured distributions are also included. Topographic data from SWLI microscope 1 were used in both calculations, and a Schwartz window was used in the phase integral calculation. The measured in-

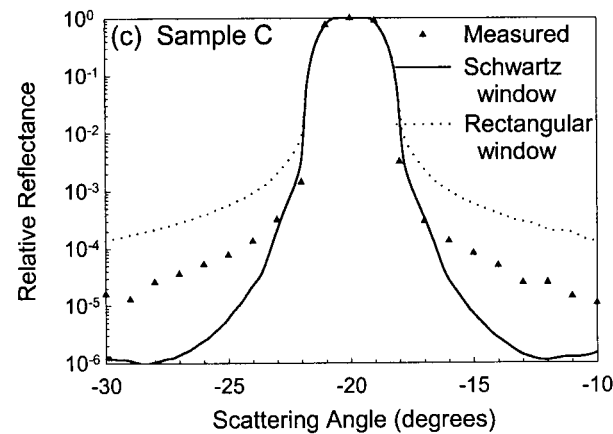
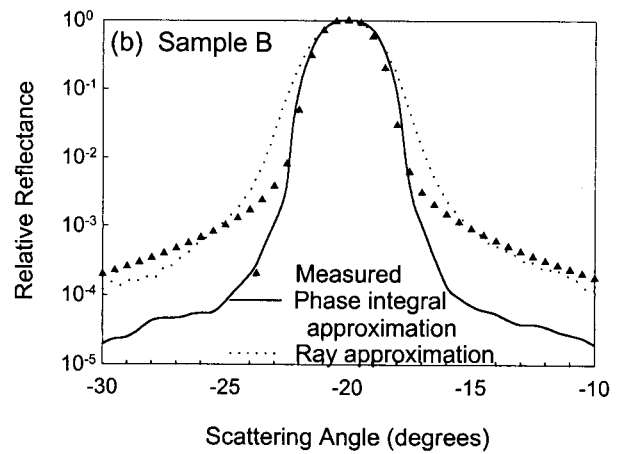
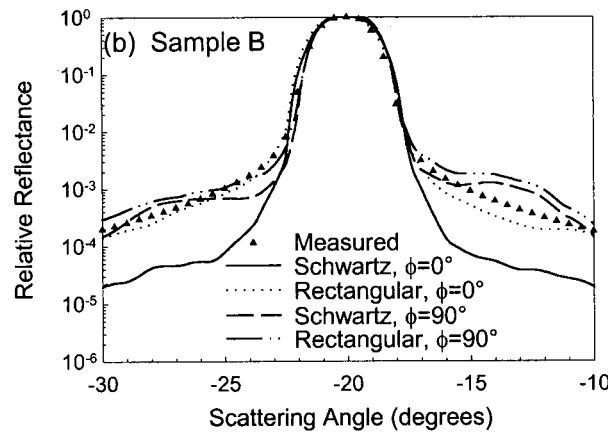
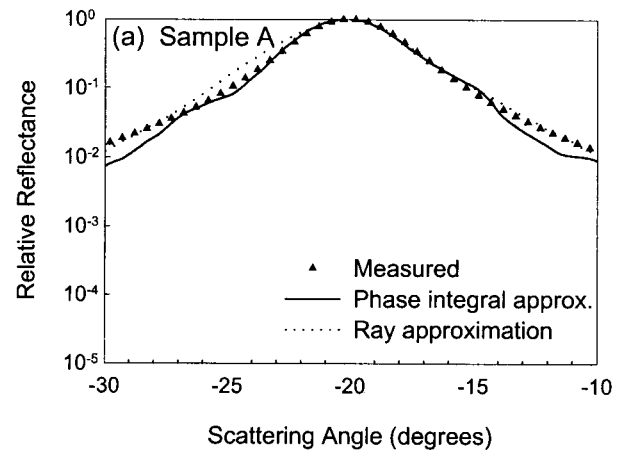
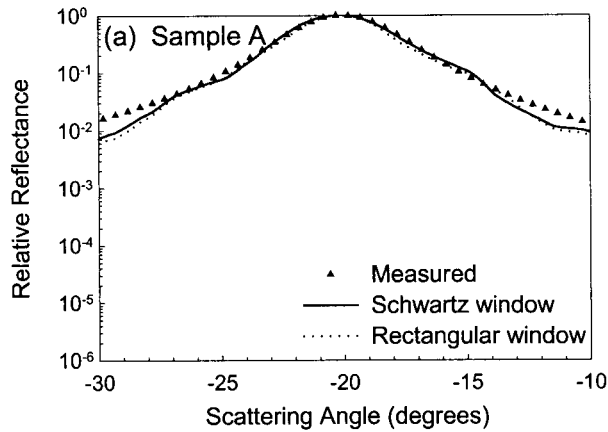


Fig. 14. Comparison of measured and computed reflectance curves, showing the difference between the phase integral and ray approximations with SWLI 1 topographical data and the Schwartz window.

Fig. 13. Comparison of measured and computed reflectance curves, showing the difference between the effects of Schwartz and rectangular windows for data taken with SWLI 1. For sample B, calculated results are shown for $\phi_i = 0^\circ$ and $\phi_i = 90^\circ$.

strument signature was not incorporated in the calculations using the ray algorithm, only the effect of the detector aperture, as discussed in Section 3. For these samples the models provide similar results.

5. Concluding Remarks

Clear dielectric isotropic coatings that have surfaces with reflectance characteristics, ranging from

strongly specular to diffuse, were used to compare calculations and measurements of angle-resolved distributions. Results were shown for the angle of incidence of 20° only. Two optical scattering approximations were used in the calculations. One is based on Kirchhoff's formalism, and the other is based on the reflection of light rays by locally flat surfaces. It was demonstrated that the phase integral obtained with Kirchhoff's formalism for the scalar wave scattering theory produces relative reflectance curves that agree fairly well with the measured curves. For the smoothest sample (C), the slow decrease of the sinc function for a large argument produces computed reflectances that exceed the measured values away from the specular direction. The discontinuity at the edges of the illuminated patch caused by the default rectangular window causes the computed intensity to remain too high at angles far from the specular beam. Consequently, the Schwartz windowing function was used to obtain the calculated intensities shown here.

The second optical scattering approximation replaces the surface by tangent planes that produce only a specular ray. It gives results similar to those

obtained from the phase integral and from the measured curves. It is a simpler approach to use computationally than the Kirchhoff formalism. For example, the running times of the program used to compute the phase integral varied between 10 and 18 CPU h on a SGI⁸ Origin 2000, whereas the computation of the ray scattering took ~6 CPU s on a SUN⁸ Ultra 30 workstation.

For the rougher epoxy sample, the agreement is good regardless of the method used to compute the relative reflectance. Also, agreement between measured and computed reflectance values justifies the use of the spline interpolation on surface maps for these surfaces, needed to perform the phase integrals.

Overall, either Kirchhoff formalism or the ray approximation can be used to simulate the visible light scatter for rough surfaces, A and B. In a separate study⁷ the ray approximation was used to perform comparative image rendering of surfaces A and B with good results. To simulate the glossiness of the surfaces as seen by an observer, the scatter distributions were computed with an angular resolution roughly equal to that of the human eye under indoor lighting conditions. Assuming that the pupil has a diameter of 4 mm and that the viewing distance is 500 mm, the subtended angle is ~0.5°. The detector aperture used here for the scattering measurements subtended an angle of 2.7°, suitable for comparing with the computed scattering results but not appropriate for simulating the response of the eye to mirrorlike reflection. If light-scattering data are to be used for image rendering of gloss, the angular resolution should also be ~0.5° or less.

The authors gratefully acknowledge the helpful discussions with our colleagues T. Nguyen and J. W. Martin and the guidance provided by T. Nguyen in preparing the samples. J. Figureoa provided the data for samples A and B with microscope 1,^{8,16} S. Kobak provided the data for samples A and B with microscope 2,^{8,17} and J. Fu provided the data for sample C with microscope 3. This research was supported in part by the NIST Director's Competence Program.

References and Note

1. M. Maynard, "Automakers' color guard not spinning its wheels," USA Today, 26 October 1998, p. 12B.
2. M. E. McKnight and J. W. Martin, "Advanced methods and models for describing coating appearance," *Prog. Org. Coat.* **34**, 152–159 (1998).
3. P. Y. Barnes, E. A. Early, and A. C. Parr, "Spectral reflectance," NIST (Nat. Inst. Stand. Technol.) Spec. Publ. 250–48 (1998).
4. P. Beckmann and A. Spizzichino, *The Scattering of Electromagnetic Waves from Rough Surfaces* (Pergamon, New York, 1963), p. 67 ff.
5. R. Brodmann and M. Algäuer, "Comparison of light scattering from rough surfaces with optical and mechanical profilometry," in *Proceedings on Surface Measurement and Characterization*, J. M. Bennett, ed., Proc. SPIE **1009**, 111–118 (1988).
6. J. T. Bendler, S. F. Feldman, H. Hatti, and S. Y. Hobbs, "Approximate model of diffuse reflectance from rough polymer surfaces," *J. Appl. Phys.* **83**, 998–1004 (1998).
7. F. Y. Hunt, E. Marx, G. W. Meyer, T. V. Vorburger, P. A. Walker, and H. B. Westlund, "A first step towards photorealistic rendering of coated surfaces and computer based standards of appearance," in *Service Life Methodology and Metrology*, J. W. Martin and D. R. Bauer, eds., ACS Symposium Series (Oxford U. Press, New York, 2001).
8. Certain commercial equipment is identified in this paper to describe adequately an experimental procedure. Such identification does not imply that the equipment identified is necessarily the best available for the purpose nor does it imply any recommendation or endorsement by NIST.
9. ASME Surface Quality Standard B46.1, *Surface Texture* (American Society of Mechanical Engineers, New York, 1995).
10. D. B. Hall, P. Underhill, and J. M. Torkelson, "Spin coating of thin and ultrathin polymer films," *Polym. Eng. Sci.* **38**, 2039–2045 (1998).
11. F. E. Nicodemus, J. C. Richmond, J. J. Hsia, I. W. Ginsberg, and T. Limperis, "Geometrical considerations and nomenclature for reflectance," Natl. Bur. Stand. (U.S.) Monogr. **160** (1977).
12. J. E. Proctor and P. Y. Barnes, "NIST high accuracy reference reflectometer-spectrophotometer," *J. Res. Natl. Inst. Stand. Technol.* **101**, 619–627 (1996).
13. P. J. Caber, "Interferometric profiler for rough surfaces," *Appl. Opt.* **32**, 3438–3441 (1993).
14. L. Deck and P. de Groot, "High-speed noncontact profiler based on scanning white-light interferometry," *Appl. Opt.* **33**, 7334–7338 (1994).
15. T. Doi, T. V. Vorburger, and P. Sullivan, "Effects of defocus and algorithm on optical step height calibration," *Proc. Eng.* **23**, 135–143 (1999).
16. WYKO NT-2000, Veeco Metrology Group, Tucson, Ariz. 85706.
17. Zygo New View 5030, Zygo Corporation, Middlefield, Conn. 06455–0448.
18. B. Bhushan, J. C. Wyant, and C. L. Koliopoulos, "Measurement of surface-topography of magnetic tapes by Mirau interferometry," *Appl. Opt.* **24**, 1489–1497 (1985).
19. K. Creath, "Comparison of phase-measurement algorithms," K. Creath, ed., Proc. SPIE **680**, 19–28 (1986).
20. E. Marx and T. V. Vorburger, "Windowing effects on light scattered by sinusoidal surfaces" in *Optical Scattering: Applications, Measurement, and Theory II*, J. C. Stover, ed., Proc. SPIE **1995**, 2–14 (1993).
21. E. Marx, T. R. Lettieri, and T. V. Vorburger, "Light scattering by sinusoidal surfaces: illumination windows and harmonics in standards," *Appl. Opt.* **34**, 1269–1277 (1995).
22. D. E. Barrick, "Grazing behavior of scatter and propagation above any rough surface," *IEEE Trans. Antennas Propag.* **46**, 73–83 (1998).
23. E. Marx, "Integral equations for scattering by a dielectric," *IEEE Trans. Antennas Propag.* **32**, 166–172 (1984).
24. J. M. Elson and J. M. Bennett, "Vector scattering theory," *Opt. Eng.* **18**, 116–124 (1979).
25. B. N. Taylor and C. E. Kuyatt, "Guidelines for evaluating and expressing the uncertainty of NIST measurement results," Natl. Inst. Stand. Technol. Tech. Note 1297 (National Institute of Standards and Technology, Washington, D.C., 1994).